



## Research paper

# Noble metal-free metal-organic framework-derived onion slice-type hollow cobalt sulfide nanostructures: Enhanced activity of CdS for improving photocatalytic hydrogen production



D. Praveen Kumar, Hanbit Park, Eun Hwa Kim, Sangyeob Hong, Madhusudana Gopannagari,  
D. Amaranatha Reddy, Tae Kyu Kim\*

Department of Chemistry and Chemical Institute for Functional Materials, Pusan National University, Busan 46241, Republic of Korea

## ARTICLE INFO

**Keywords:**  
Hollow nanostructures  
Photocatalysis  
Hydrogen  
 $\text{Co}_4\text{S}_3/\text{CdS}$   
Metal-organic framework

## ABSTRACT

The hollow materials have played a significant role in cutting-edge innovations for energy conversion due to their peculiar properties and their wide range of potential applications. These materials show great promise for the development of cleaner power sources to address growing environmental concerns at a time of increasing global demand for energy. Noble metal-free MOF-derived onion slice-type hollow structured  $\text{Co}_4\text{S}_3$  was developed and embedded with CdS nanoparticles for photocatalytic hydrogen production. The incorporation of  $\text{Co}_4\text{S}_3$  with the CdS particles effectively accelerated charge separation and transfer in photocatalytic reactions due to the low density, hollow interior, and shell permeability of the onion-type composite. The optimized  $\text{Co}_4\text{S}_3/\text{CdS}$  photocatalyst led to an enhanced rate of  $\text{H}_2$  production of  $12,360 \mu\text{mol h}^{-1} \text{g}^{-1}$  under simulated solar light irradiation; this value is 26-fold greater than that of the pristine CdS nanoparticles. The  $\text{Co}_4\text{S}_3/\text{CdS}$  composite exhibited remarkably stable photocatalytic performance for up to 65 h and could be reused in five successive cycles. Furthermore, to the best of our knowledge, this is the highest  $\text{H}_2$  production rate achieved with cobalt sulfide-based CdS nanoparticle photocatalysts in the photocatalysis of water under simulated solar light irradiation. Owing to its low cost and high efficiency, this photocatalytic system should hold great potential for the development of highly efficient photocatalytic materials for use in various fields.

## 1. Introduction

The global energy crisis and environmental issues have fueled intensive research towards the realization of the hydrogen economy. Economically feasible strategies for storage of the produced hydrogen remain critically important for widespread use of hydrogen as an energy source [1,2]. Hydrogen energy is regarded as “green” energy because of the high efficiency and eco-friendliness of hydrogen combustion. Hydrogen, regarded as a perfect energy source, is thought to be a promising alternative to fossil fuels that can be implemented within the foreseeable future because of its high energy and carbon-free nature [3]. Various methods have been developed for the production of hydrogen as a fuel and for solar energy utilization. Artificial photosynthesis has been the focus of intensive research effort due to its unmatched resource potential. Recently, the search for earth-abundant catalysts as replacements for expensive and rare precious metals has intensified. Several photocatalytic materials have been investigated, including  $\text{TiO}_2$  [4–8],  $\text{ZnO}$  [9–12],  $\text{C}_3\text{N}_4$  [13–15], and CdS [16–21].

Among the various visible-light-active semiconductor photocatalysts, CdS has gained prominence as an appropriate candidate for photocatalytic water splitting because of its well-suited band-gap of ca. 2.4 eV that facilitates superb excitation of charge carriers via effective absorption of solar light. The conduction band-edge potential of CdS is more negative than the reduction potential of  $\text{H}_2\text{O}/\text{H}_2$ , which is favorable for the reduction of protons to  $\text{H}_2$  gas [22–25]. However, the greatest energy production efficiency for photocatalytic water splitting achieved to date is far below that required for practical applications. This is attributable to the fast recombination of the photoinduced electron–hole pairs in the photocatalysts and their susceptibility to photo-corrosion [26]. The modification of existing photocatalysts to enhance their photocatalytic activity in various ways has also been explored. One successful approach involves the loading of co-catalysts onto the surface of photocatalysts; a co-catalyst is usually required to trap the photo-generated electrons from the photoactive photocatalyst. This might not entirely suppress electron–hole recombination, but may reduce the energy required for the surface reaction. Noble metals are

\* Corresponding author.

E-mail address: [tkkim@pusan.ac.kr](mailto:tkkim@pusan.ac.kr) (T.K. Kim).

usually considered the most robust co-catalysts [27–30]. However, their high value and scarcity impede their widespread use, making earth-abundant metals and their compounds attractive alternatives.

Recently, transition metal sulfides (TMS) with various compositions, crystal structures, valence states, and nanocrystalline morphologies that exhibit enhanced electrochemical activity have been successfully fabricated [31–33]. TMSs typically possess higher electrical conduction and mechanical and thermal stability than their corresponding metal oxide counterparts [32,34]. Among the TMSs, Co-based sulfides have emerged as promising co-catalytic materials for photocatalytic applications because of their many advantages, such as their higher electrical conductivity and richer redox reactions than those of the corresponding oxides and hydroxides. The construction of interesting hollow structures in existing materials has also been considered to be vital for boosting the photocatalytic performance of these materials. Hollow-structured nanomaterials have attracted significant attention because of their distinctive interior voids, low density, large surface area, and reduced transport lengths for mass and charge transport [35–38]. Multi-shelled hollow nanostructures offer superior benefits for different applications. Multi-shelled structures are beneficial for achieving enhanced energy density due to the higher content of active species. Specifically, zero-dimensional nanoparticles can be readily dispersed in hollow nanostructures. Nano-sized subunits can significantly shorten the transport distance of ions, making rapid charge and discharge possible. However, the development of hollow nanostructures in the required manner remains a great challenge because of the difficulties associated with delicate control of the chemical reactions and the structural compatibility of different subunits on the nanoscale.

Metal–organic frameworks (MOFs) are porous crystalline inorganic–organic hybrid materials that have attracted great interest in recent years. MOFs offer great promise, especially in the fabrication of metal sulfide hollow nanostructures. Hu et al. [39] reported a MOF-based approach for forming hierarchical double-shelled hollow structures with CoS-nanosheet-constructed shells on CoS-nanoparticle-assembled nanoboxes for supercapacitors. Yu et al. [40] synthesized cubic NiS nanoframe-like hollow structures by anion exchange of Ni–Co Prussian blue analogue nanocubes with  $S^{2-}$  ions in a metal–organic framework for electrochemical applications. Guan et al. [41] explained the preparation of onion-like cobalt oxide particles that were transformed into onion-like cobalt sulfide particles with hollow-structured shells via an anion-exchange reaction between cobalt oxide and  $S^{2-}$  ions for use in supercapacitor applications. These experiments showed that Co-based sulfide is a promising substitute for noble metals for photocatalytic applications.

Herein, we report the preparation of earth-abundant onion slice-type cobalt sulfide nanostructure networked CdS nanoparticles ( $Co_4S_3/CdS$ ) by simple methods. The synthesized materials are applied to photocatalytic hydrogen evolution under simulated solar light irradiation with lactic acid as a hole-scavenger under the optimized conditions. The  $Co_4S_3/CdS$  material exhibits a high rate of  $H_2$  production ( $12,360 \mu\text{mol h}^{-1} \text{g}^{-1}$ ); the onion slice-type cobalt sulfide nanostructures along with CdS nanoparticles effectively separate the photo-generated charge carriers and improve the surface shuttling properties for efficient  $H_2$  production. To the best of our knowledge, this material shows the best performance among all reported cobalt sulfide-based co-catalyst CdS composites (Table S1 in Supplementary materials).

## 2. Experimental and characterizations

### 2.1. Materials

Cadmium acetate dihydrate ( $Cd(CH_3COO)_2 \cdot 2H_2O$ ), cobalt nitrate ( $Co(NO_3)_2 \cdot 6H_2O$ ), isophthalic acid (IPA), dimethylformamide (DMF), acetone, sodium sulfide ( $Na_2S$ ) and ethanol were obtained from Alfa Aesar. All chemicals were used without further purification.

### 2.2. Synthesis of Co-MOFs

All chemicals were of analytical grade and were used without further purification. In a typical procedure, for the preparation of Co-MOF first, 10 mL (0.1 mmol) of cobalt nitrate ( $Co(NO_3)_2 \cdot 6H_2O$ ) and 10 mL (0.1 mmol) of isophthalic acid (IPA) were dissolved in a mixture of DMF and acetone (5 mL + 5 mL); the mixture was magnetically stirred for 6 h to form a clear solution. The solution was then transferred to a 50 mL Teflon cup and heated in an autoclave at 160 °C for 4 h. After cooling to room temperature, the product was separated by centrifugation at 1000 rpm for 10 min and dried at 80 °C for 12 h. The obtained Co-MOF was calcined in air at 500 °C for 10 min at a heating rate of 5 °C/min<sup>-1</sup> to form  $Co_3O_4$ . According to Guan et al. [41], onion slice type nanostructures were formed from Co-MOF through the effect of heterogeneous contraction with thermal decomposition. The main reason for the formation of onion slice shaped nanostructures was due to huge volume/mass reduction from Co-MOF to metal oxide. The thermal treatment causes decomposition of amorphous Co-based coordination polymer (Co-CPS) to form a layer of  $Co_3O_4$  on the surface of the Co-CPS, and further leads to spallation when the  $Co_3O_4$  layer reaches a critical thickness. With prolonged heating, the same contraction process repeats and finally a  $Co_3O_4$  particle is formed.

### 2.3. Synthesis of $Co_4S_3$ sulfide from $Co_3O_4$

In the typical procedure for preparation of the cobalt sulfide ( $Co_4S_3$ ) nanoparticles,  $Co_3O_4$  particles were first suspended in 10 mL of 0.3 M  $Na_2S$  solution. The mixed solution was transferred to a Teflon-lined stainless steel autoclave and kept at 90 °C for 24 h. After cooling to room temperature, the product was separated by centrifugation, washed with deionized water and ethanol, and finally dried at 80 °C for 12 h.

### 2.4. Synthesis of CdS nanoparticles

Equimolar (0.1 M, 20 mL) solutions of cadmium acetate ( $Cd(OAc)_2$ ) and  $Na_2S$  were prepared, and  $Na_2S$  was slowly added dropwise to the  $Cd(OAc)_2$  solution with magnetic stirring. A yellow precipitate was obtained, washed many times with distilled water and ethanol, and dried at 80 °C for 12 h.

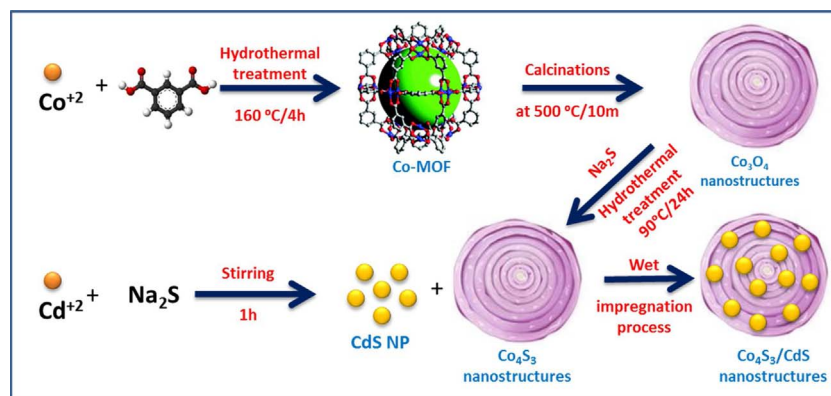
### 2.5. Synthesis of $Co_4S_3/CdS$ composite

$Co_4S_3$  decorated with CdS nanoparticles was prepared by the wet chemical method described in our previous paper [8]. In a typical preparation, 0.1 g of CdS NPs and the required amount of  $Co_4S_3$  nanoparticles were suspended in 10 mL of ethanol in a 50 mL glass beaker. The mixture was stirred for 30 min and allowed to dry at 80 °C for 12 h. A schematic representation of the material preparation process is shown in [Scheme 1](#).

## 3. Results and discussion

### 3.1. Structural analyses

The phase compositions and structures of the as-synthesized materials investigated by powder X-ray diffraction (XRD). The XRD pattern consents the formation of Co-MOF, then the mild calcination of Co-MOF converts into  $Co_3O_4$  and the diffraction pattern of  $Co_3O_4$  was confirms the formation of cubic spinel  $Co_3O_4$  phase, it was well matched with JCPDS card No. 42-1467 (Fig. S1) [41]. This  $Co_3O_4$  was converted into  $Co_4S_3$  by ion exchange and it confirms the formation of a mixed hexagonal  $Co_4S_3$  (JCPDS-02-1458) and face-centered cubic  $Co_4S_3$  (JCPDS-02-1338) with well-defined characteristic (311), (222), (331), and (511) reflections of cubic  $Co_4S_3$  and the (100), (101), (102), (003), and (110) planes of the hexagonal  $Co_4S_3$  phase (Fig. S2). The diffraction



**Scheme 1.** Schematic representation of material preparation: synthesis of Co-MOFs, synthesis of cobalt sulfide derived from Co-metalloc-organic framework and synthesis of  $\text{Co}_4\text{S}_3/\text{CdS}$  composite.

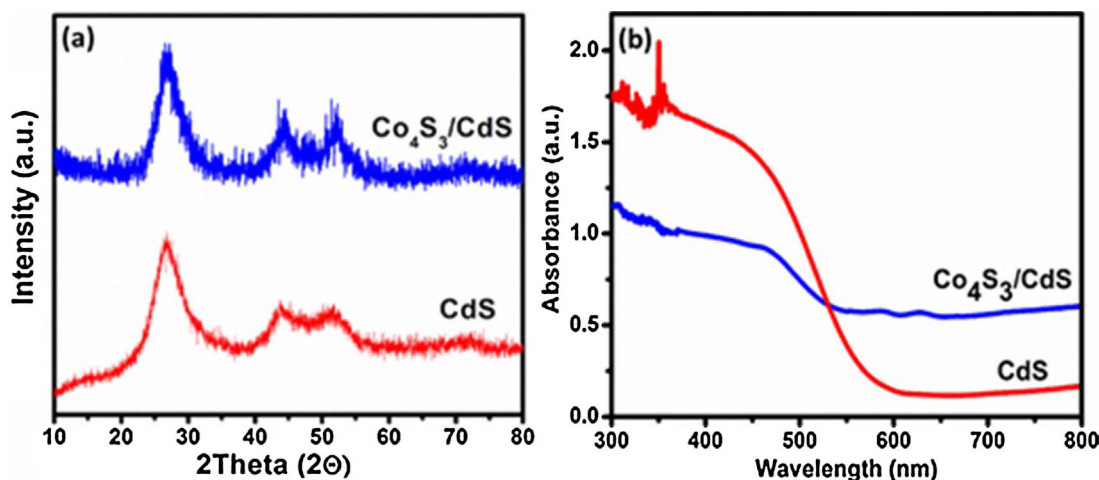


**Fig. 1.** (a) XRD patterns and (b) UV/Vis diffuse reflectance spectra of CdS and  $\text{Co}_4\text{S}_3/\text{CdS}$  composites.

patterns of the CdS nanoparticles and  $\text{Co}_4\text{S}_3/\text{CdS}$  composites are displayed in Fig. 1(a), corresponding to the face-centered cubic phase of CdS (JCPDS No. 80-0019). No obvious characteristic diffraction peaks of  $\text{Co}_4\text{S}_3$  were found, which could be attributed to the relatively low content and weak diffraction intensity of  $\text{Co}_4\text{S}_3$ .

### 3.2. DRS UV analysis

The optical properties of CdS and its composite materials were studied by UV visible diffuse reflectance spectroscopy (DRS). As shown in Fig. 1(b), the band-edge positions of CdS and the composites were located at around 575 nm, but the capacity for visible light absorption was higher for the composite. The enhanced absorption capability might be ascribed to the effect of the better interaction with light, which is induced by the added co-catalyst  $\text{Co}_4\text{S}_3$  [42]. The zero-dimensional CdS nanoparticles can be readily dispersed in hollow onion slice type nanostructures, thus facilitating the visible light absorption capability of the nanocomposite. The band-gaps of the CdS and  $\text{Co}_4\text{S}_3/\text{CdS}$  nanocomposites were calculated to be 2.0 eV (Fig. S3), indicating their similarity to that of pure CdS. On the other hands, the band gap of pure  $\text{Co}_4\text{S}_3$  was estimated to be 1.75 eV. These results confirm that the as-synthesized nanocomposites have a higher capacity to utilize solar irradiation, which leads to better photocatalytic efficiency than that of the pure CdS nanoparticles.

### 3.3. Morphological analysis

The morphology of the synthesized materials investigated by field-emission scanning electron microscopy (FESEM) (Fig. 2). Fig. 2(a) shows the spherical morphology of the synthesized Co-MOF material.

$\text{Co}_3\text{O}_4$  was obtained by calcination of Co-MOF; the morphology was influenced by the hollow structure of the MOF, as shown in Fig. 2(b).  $\text{Co}_3\text{O}_4$  was converted into  $\text{Co}_4\text{S}_3$  via ion exchange (Fig. 2(c)) [41]. The morphology of the  $\text{Co}_4\text{S}_3/\text{CdS}$  composite also displayed in Fig. 2(d) and (f). The red circles in the images indicate  $\text{Co}_4\text{S}_3$  in the composite with the CdS nanoparticles. The elemental compositions determined by energy-dispersive X-ray spectroscopy (EDS) are displayed in Fig. 2(f), confirming the presence of three elements: Cd, Co and S elements. The EDS results confirmed that CdS nanoparticles were embedded on the  $\text{Co}_4\text{S}_3$  hollow structures. The morphology of the synthesized  $\text{Co}_4\text{S}_3/\text{CdS}$  composite was investigated by transmission electron microscopy (TEM) analysis (Fig. 3). Fig. 3(a) and (b) shows the TEM images of bare  $\text{Co}_4\text{S}_3$ , demonstrating its onion slice-type morphology. The red circles in the image are onion slice-type layers. Fig. 3(c)–(e) confirm the presence of hollow spaces in the spheres, like an onion slice. The red circles in the images represent  $\text{Co}_4\text{S}_3$  and the yellow arrows and circles indicate the CdS nanoparticles, confirming the  $\text{Co}_4\text{S}_3$  nanostructures with embedded CdS nanoparticles. The elemental compositions determined by EDS mapping are displayed in Fig. 3(f), confirming the presence of three elements: Cd, Co, and S elements. EDS results indicated that CdS nanoparticles were embedded in the  $\text{Co}_4\text{S}_3$  hollow structures.

### 3.4. Surface elemental analysis

The X-ray photoelectron spectroscopy (XPS) is a particularly useful tool for studying the surface composition and electronic structure of materials, and provides information about the chemical environment of the elements in the synthesized composites. XPS analysis was used to determine the chemical states of Cd, Co, and S in the as-prepared  $\text{Co}_4\text{S}_3/\text{CdS}$  composite. Results are displayed in Fig. 4(a)–(d). The XPS

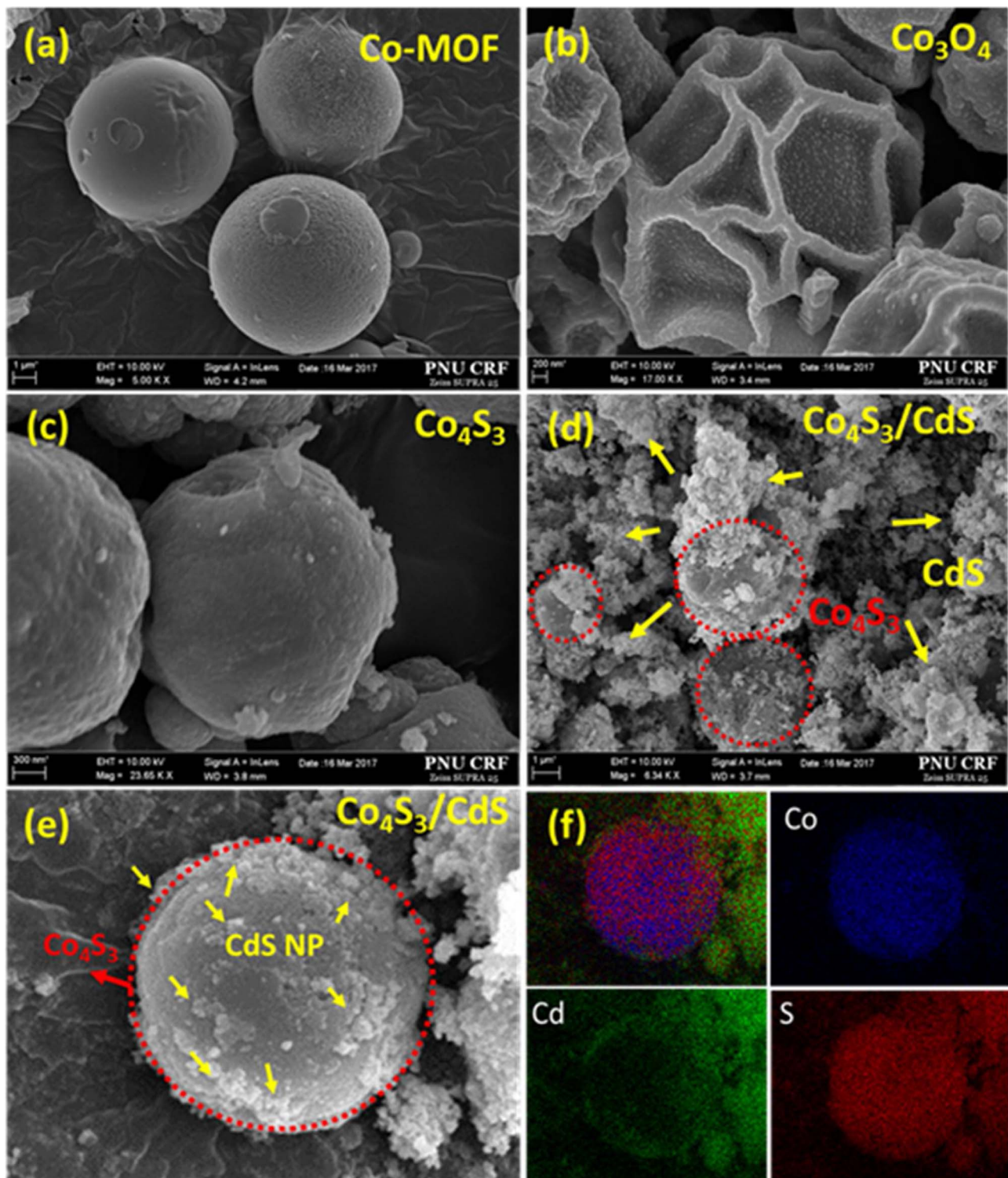


**Fig. 2.** FESEM images of (a) Co-MOF, (b)  $\text{Co}_3\text{O}_4$ , (c)  $\text{Co}_4\text{S}_3$ , (d)  $\text{Co}_4\text{S}_3/\text{CdS}$ , (e) high-magnification FESEM images of  $\text{Co}_4\text{S}_3/\text{CdS}$ , and (f) elemental analysis of  $\text{Co}_4\text{S}_3/\text{CdS}$  (Cd, S, and Co elements).

survey spectrum (Fig. 4(a)) reveals the presence of Cd, Co, S, C and O elements in the nanocomposites. The oxidation states of these elements were confirmed from the high-resolution Cd 3d, S 2p, and Co 3d XPS spectra. The Cd 3d XPS spectrum (Fig. 4(b)) shows peaks at binding energies of 404.6 and 411.3 eV, corresponding to Cd 3d<sub>5/2</sub> and 3d<sub>3/2</sub> transitions, respectively. This result confirms that Cd was in the +2 oxidation state in CdS [20]. In addition, S 2p peaks (Fig. 4(c)) were detected at 161.19 and 162.7 eV, and Co 3d peaks (Fig. 4(d)) were

appeared at 778.3 (Co 2p<sub>3/2</sub>) and 796.6 eV (Co 2p<sub>1/2</sub>). These Co and S peaks confirmed the formation of  $\text{Co}_4\text{S}_3$  [41].

### 3.5. Photoluminescence spectral analysis

Photoluminescence (PL) measurement used to evaluate the electronic transitions in the photocatalyst system. The emission spectra were recorded in the range of 100–1000 nm after irradiation at an

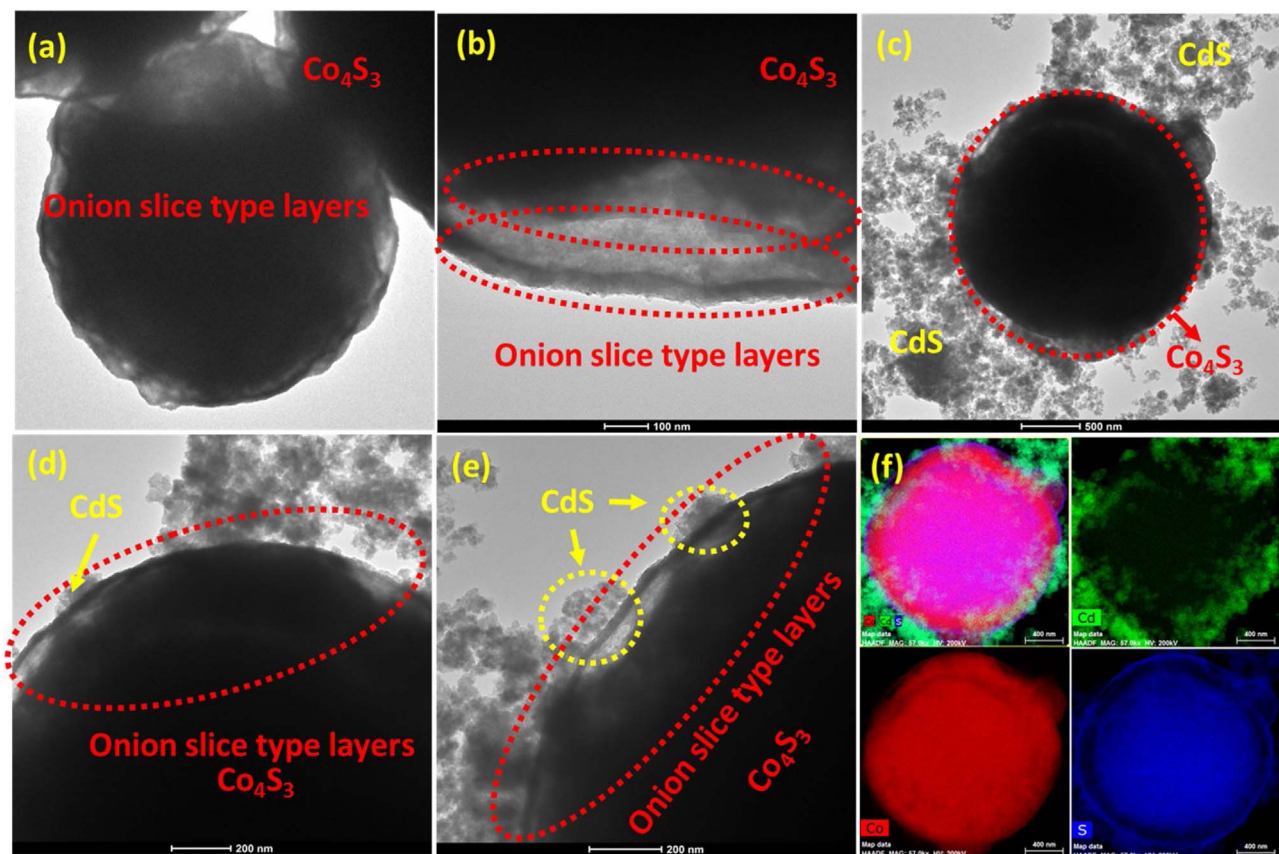


Fig. 3. (a)–(c) TEM images of Co<sub>4</sub>S<sub>3</sub>/CdS and (d) elemental analysis of Co<sub>4</sub>S<sub>3</sub>/CdS (Cd, S, and Co elements).

excitation wavelength of 380 nm. Fig. 5(a) shows the PL spectra of CdS and Co<sub>4</sub>S<sub>3</sub>/CdS. CdS shows distinct bands, probably associated with near-band-edge emission, whereas the emissions of CdS are attributed to surface defects. [20] According to a previous study [17,18], the photogenerated carriers are easily transferred to the surface, where electrons are not available for H<sub>2</sub> evolution processes. After CdS nanoparticles embedded into onion slice type hallow Co<sub>4</sub>S<sub>3</sub> nanostructures, the intensity of the PL emission bands decreased (Fig. 5(a)), suggesting fast photoinduced electron transfer due to these multi-shells can significantly shorten the transport distance of ions, making rapid charge and discharge possible. Moreover, the weakened intensity of the emission bands indicates that most of the surface states were passivated, thereby making electrons available for photocatalytic H<sub>2</sub> evolution. The emission bands of Co<sub>4</sub>S<sub>3</sub>/CdS were significantly less intense than pure CdS, implying that Co<sub>4</sub>S<sub>3</sub> facilitates the charge carrier transfer processes (making them faster) due to the increased number of surface active sites and improved conductivity with multi-shelled [42].

### 3.6. Photoelectrochemical (PEC) analysis

To further support the enhanced separation efficiency and charge carrier transport capabilities of as-synthesized nanocomposites, indium tin oxide (ITO) electrodes coated with CdS (and Co<sub>4</sub>S<sub>3</sub>/CdS nanocomposites) were photoelectrochemically examined under simulated sunlight irradiation using a potentiostat. Fig. 5(b) shows the photocurrent responses of the bare CdS nanostructures and the related nanocomposites with 30 s on/off irradiation cycles during the period of 360 s. As shown in Fig. 5(b), the photocurrent intensity of the Co<sub>4</sub>S<sub>3</sub>/CdS nanocomposites was higher than that of the bare CdS nanoparticles, suggesting greater separation efficiency of the photoexcited electron-hole pairs in the former due to onion shaped multi-shells, which can significantly shorten the transport distance of ions, making

rapid charge and discharge possible. The photocurrent intensity of the Co<sub>4</sub>S<sub>3</sub>/CdS nanocomposites was very slightly decline initially up to 150 s possibly due to establishing equilibrium in between electrolyte solution and synthesized material ITO coated electrode layer upon instant exposure to solar irradiation source. Consequently, the stable photocurrent response was observed for long time up to 360 s. Iqbal et al. [46] also observed declined photocurrent responses at initial time for the case of GaON material, which is in good agreements with our results. Moreover, the photocurrent responses were highly reproducible for several on/off cycles and remained stable, indicating that the Co<sub>4</sub>S<sub>3</sub> with CdS could effectively prevent photocorrosion. These observations were well supported by the PL data. Based on the above experimental evidence, one can envision that the hollow Co<sub>4</sub>S<sub>3</sub> nanostructures can effectively enhance the photocatalytic activity of the CdS nanoparticles. In addition, as shown in Fig. S6, the Nyquist plots attained from electrochemical impedance spectroscopy (EIS) measurements. In these plots, CdS and Co<sub>4</sub>S<sub>3</sub>/CdS nanocomposite show the typical semicircles at high frequencies. Co<sub>4</sub>S<sub>3</sub>/CdS unveils the smaller semicircle diameter than CdS, representing that Co<sub>4</sub>S<sub>3</sub> has a superior competence to endorse the transfer of photogenerated electrons from CdS compared to bare CdS nanoparticles.

The surface area of photocatalyst plays a vital role on the rate of photocatalytic hydrogen evolution via generation of charge carriers. The reduction tendency of photogenerated electrons strappingly be contingent on migration and the separation efficiency. To endorse the role of surface area for extraordinary rate of H<sub>2</sub> production, we examined the specific surface areas of CdS and Co<sub>4</sub>S<sub>3</sub>/CdS nanocomposite by nitrogen adsorption–desorption curves (Fig. S4). The isotherms for CdS, and Co<sub>4</sub>S<sub>3</sub>/CdS are virtually identical with a type IV isotherm through a hysteresis loop at a high relative pressure (0.7–1.0), signifying the existence of mesoporous structures in the synthesized nanostructures. Based on the Brunauer–Emmett–Teller (BET) method, the

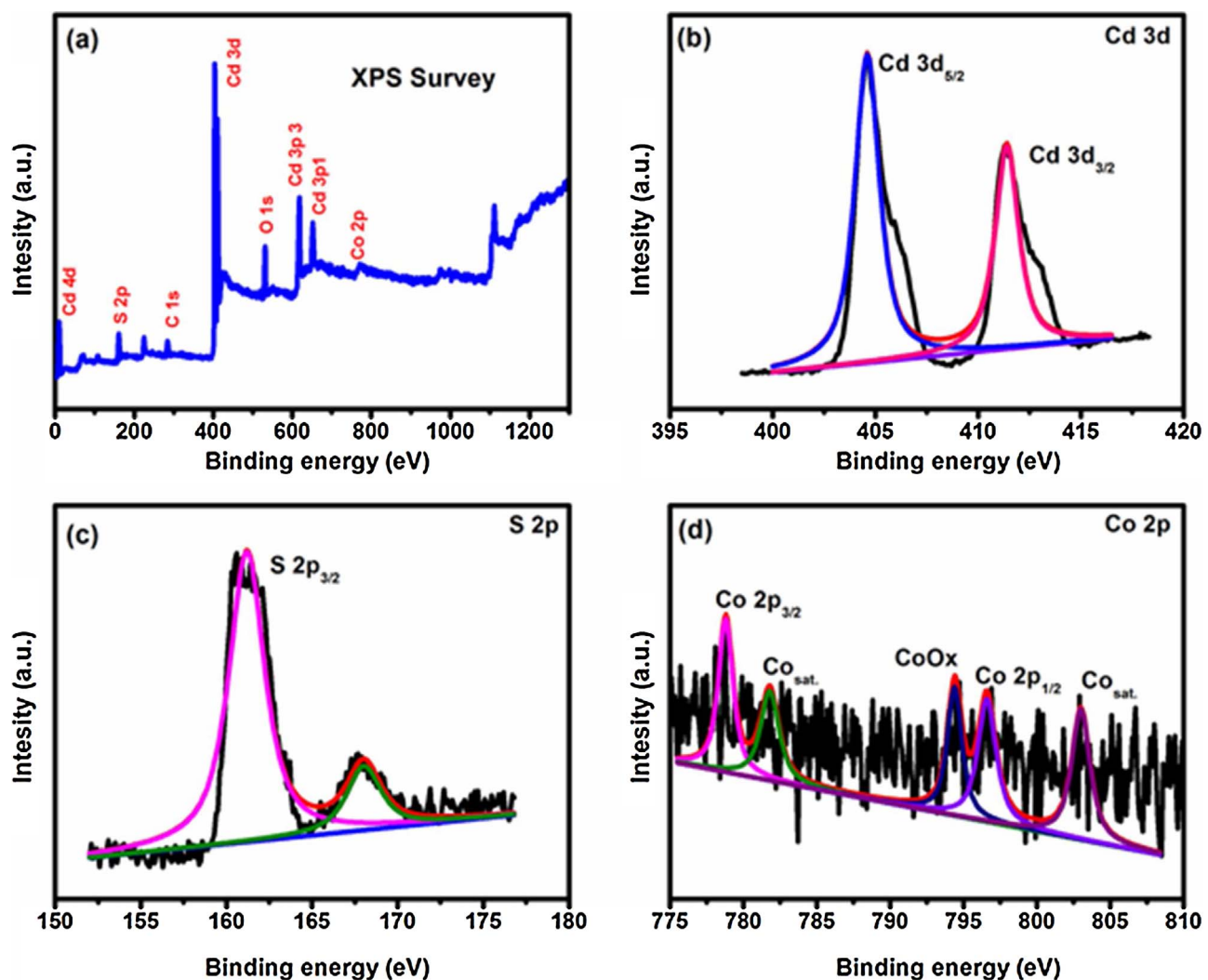


Fig. 4. XPS analysis of images of  $\text{Co}_4\text{S}_3/\text{CdS}$ : (a) XPS survey spectrum and (b)–(d) XPS spectra of Cd 3d, S 2p and Co 2p regions, respectively.

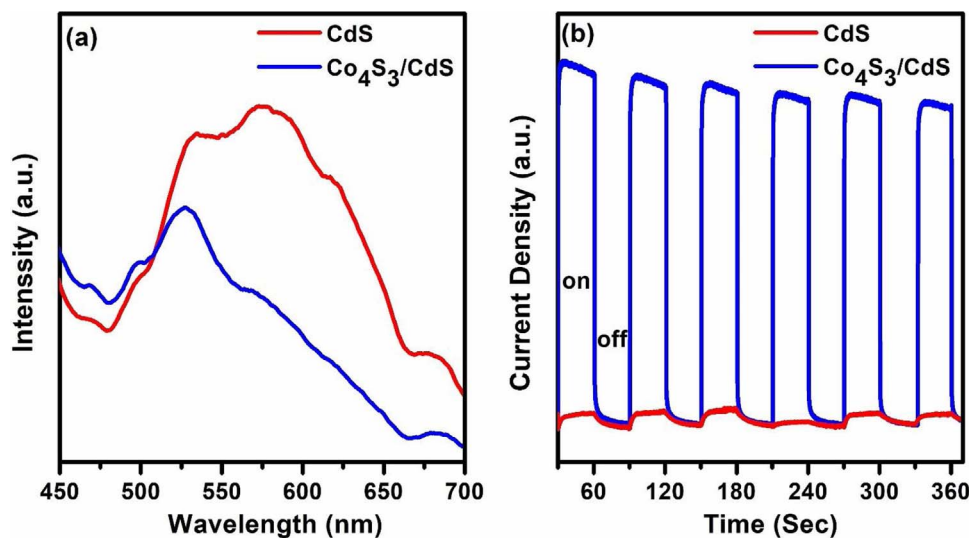
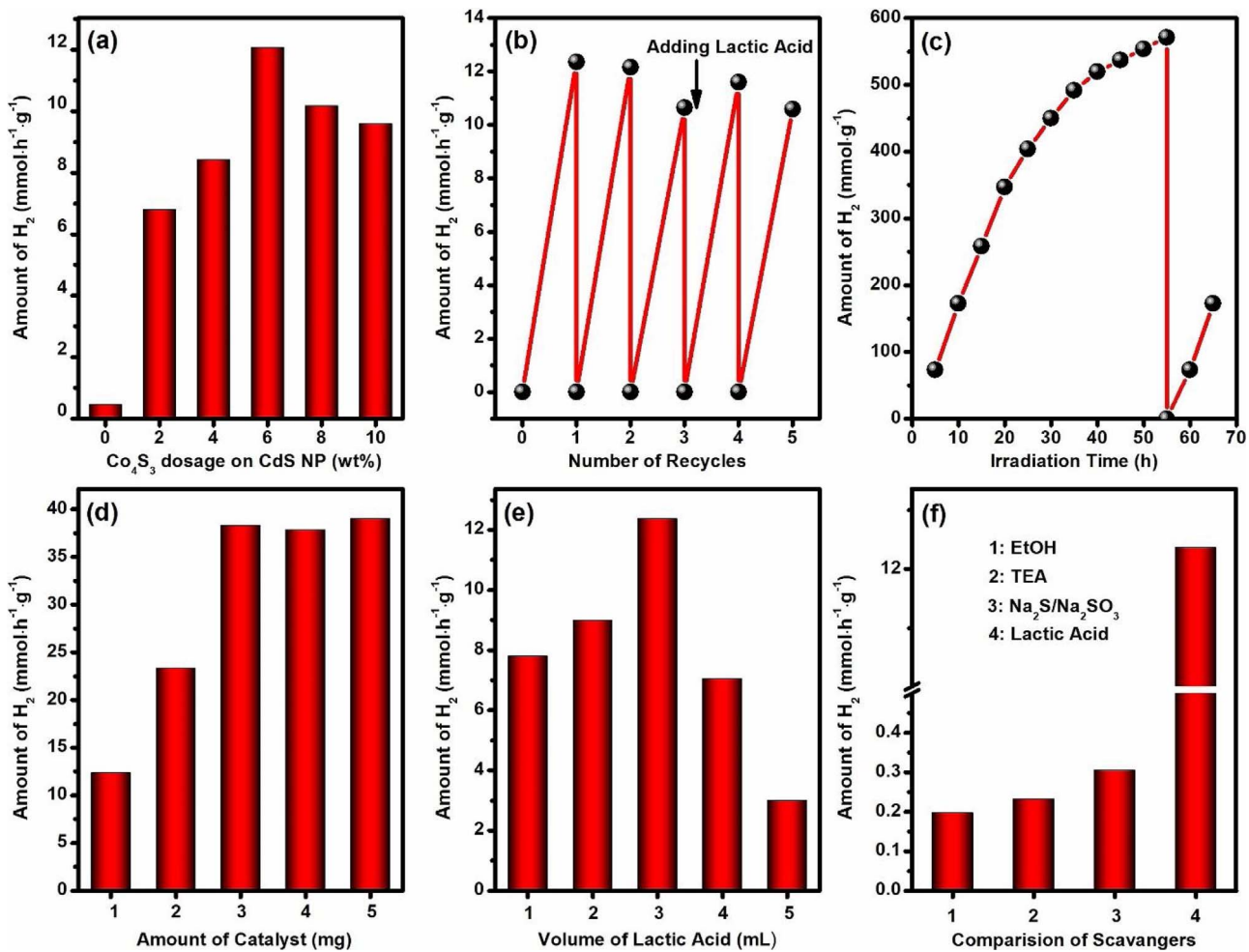


Fig. 5. (a) Photoluminescence (PL) and (b) photoelectrochemical analyses of CdS and  $\text{Co}_4\text{S}_3/\text{CdS}$  composites.

surface area of the  $\text{Co}_4\text{S}_3/\text{CdS}$  nanocomposite ( $73.974 \text{ m}^2 \text{ g}^{-1}$ ) is greatly higher than the bare CdS nanoparticles ( $53.892 \text{ m}^2 \text{ g}^{-1}$ ). The higher surface area of  $\text{Co}_4\text{S}_3/\text{CdS}$  was due to onion slice type hollow nanostructures, offering an enhanced energy density due to the higher content of active species with multi-shelled nature. This higher specific

surface area may result in a greater number of reactive sites to promote hydrogen evolution during the photocatalytic reaction.



**Fig. 6.** (a) Photocatalytic H<sub>2</sub> production studies: (a) effect of co-catalyst Co<sub>4</sub>S<sub>3</sub> weight percentage on CdS, (b) recyclability study of Co<sub>4</sub>S<sub>3</sub>/CdS, (c) long-term stability of Co<sub>4</sub>S<sub>3</sub>/CdS for 1 mg of catalyst dispersed in 15 mL of 20 vol.% aqueous lactic acid solution under simulated solar light irradiation, (d) effect of catalyst amount for Co<sub>4</sub>S<sub>3</sub>/CdS composite on hydrogen production in 15 mL of 20 vol.% aqueous lactic acid solution, (e) effect of lactic acid concentration on H<sub>2</sub> production rate of Co<sub>4</sub>S<sub>3</sub>/CdS (1 mg) and (f) effect of scavenger on H<sub>2</sub> production rate of Co<sub>4</sub>S<sub>3</sub>/CdS (1 mg).

### 3.7. Photocatalytic activity

#### 3.7.1. Effect of Co<sub>4</sub>S<sub>3</sub> weight percentage on CdS nanoparticles

The photocatalytic activity of the synthesized materials was assessed by using lactic acid as a scavenger under simulated solar light irradiation. First, the optimum weight percentage of Co<sub>4</sub>S<sub>3</sub> in the Co<sub>4</sub>S<sub>3</sub>/CdS nanocomposites was determined, as displayed in Fig. 6(a). The simultaneous presence of Co<sub>4</sub>S<sub>3</sub> and CdS greatly influences the rate of H<sub>2</sub> production, which increased with an increase in the amount of Co<sub>4</sub>S<sub>3</sub> up to an optimum level of 6.0 wt.%, followed by a decrease at higher loadings. At the optimized loading, the rate of H<sub>2</sub> production was 12,360  $\mu\text{mol h}^{-1} \text{g}^{-1}$ , which is significantly higher than the rate for the pure CdS nanoparticles (450  $\mu\text{mol h}^{-1} \text{g}^{-1}$ ). The enhanced rate of H<sub>2</sub> production could be ascribed to beneficial properties of onion slice type natures of Co<sub>4</sub>S<sub>3</sub> as achieving enhanced energy density due to the higher content of active species. As shown before, zero-dimensional CdS nanoparticles can be readily dispersed in hollow nanostructures and high electrical conductivity of Co<sub>4</sub>S<sub>3</sub> lead to effective separation of the photogenerated charge carriers and improve the surface shuttling properties. Lai et al. [36] clearly suggested the importance of hollow micro-/nano-structured shell type materials for applications in energy-related systems. These unique structures affords a superior surface-to-volume ratio and reduced transport lengths for both mass and charge transportation to surface for redox reactions. Lower Co<sub>4</sub>S<sub>3</sub> weight percentages resulted in lower rates of H<sub>2</sub> production due to the fewer

number of catalytically active sites and reduced electrical conductivity. Increasing the weight percentage of Co<sub>4</sub>S<sub>3</sub> above the optimum level (i.e., > 6.0% Co<sub>4</sub>S<sub>3</sub>) resulted in a decrease in the H<sub>2</sub> evolution rate. This decline in the activity can be explained as follows. Coverage of the CdS surface by excess Co<sub>4</sub>S<sub>3</sub> prevents exposure to the incident light and the generation of electrons from CdS, where the excess Co<sub>4</sub>S<sub>3</sub> possibly acts as a recombination center for the photogenerated electron-hole pairs [42].

#### 3.7.2. Stability and durability measurement

Recycling experiments were carried out to evaluate the stability of the Co<sub>4</sub>S<sub>3</sub>/CdS photocatalyst; the results displayed in Fig. 6(b). The H<sub>2</sub> production rate with the optimized catalyst (6 wt.% Co<sub>4</sub>S<sub>3</sub>/CdS) was evaluated over five cycles with 5 h of irradiation using simulated solar light. Almost identical amounts of H<sub>2</sub> was produced in all five experiments, although a minor increase was detected after the second cycle due to better adsorption of the reaction solution on the catalyst after the first cycle. In the cases of third and fourth cycles, we found a minor decrease in the H<sub>2</sub> production rate. It was attributed to the decrease in the lactic acid concentration via conversion to pyruvic acid during the reaction [43]. After third cycle, an additional 3 mL of lactic acid solution added, and the experimental results of the fourth cycle were similar to those of the first cycle. Thus, the catalyst was confirmed to be stable over five cycles. The long-term photo-exposure of the optimized materials for up to 65 h was monitored as shown in Fig. 6(c). The results

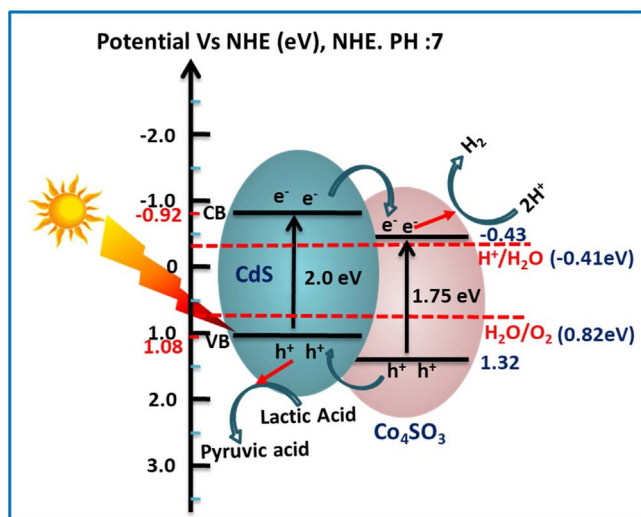


Fig. 7. Schematic representation of the proposed reaction mechanism for photocatalytic  $H_2$  production of  $Co_4S_3/CdS$  composite.

show that the rate of  $H_2$  production increased with time up to 50 h and then reached saturation. At saturation, the reactor was evacuated and the experiment was continued for 10 h. The activity was the same as in the first 10 h, hence providing strong evidence that the prepared catalyst is stable. These stable rate of hydrogen production of  $Co_4S_3/CdS$  composite is due to multi-layered onion shaped structures of  $Co_4S_3$  are highly beneficial for zero-dimensional  $CdS$  nanoparticles to readily dispersion in multi-shells without undergo corrosion.

### 3.7.3. Control measurements

Experiments on photocatalytic assessments were conducted with different amounts (1–5 mg) of the optimized  $Co_4S_3/CdS$  catalyst in 15 mL of the reaction solution. As expected, the rate of  $H_2$  production varied significantly based on the amount catalyst in the reaction solution. The rate of  $H_2$  production with 1, 2, and 3–5 mg of the photocatalyst was 12,360, 24,800 and 36,000  $\mu\text{mol h}^{-1} \text{g}^{-1}$  respectively. The  $H_2$  production rate was saturated when the catalyst amount exceeded 3 mg in 15 mL of reaction solution due to the high amount of catalyst, which exerted a shielding effect on the suspended catalyst nanocomposites [3]. The results are displayed in Fig. 6(d). The effect of the scavenger concentration on the rate of  $H_2$  production using the optimized  $Co_4S_3/CdS$  catalyst was evaluated, as shown in Fig. 6(e). Initially, the rate of  $H_2$  production was proportional to the concentration of lactic acid (for up to 3 mL in 15 mL of reaction solution, the maximum  $H_2$  production rate was 12,360  $\mu\text{mol h}^{-1} \text{g}^{-1}$ ). Subsequently, the relationship between the scavenger concentration and the hydrogen production rate became indirectly proportional. This decrease in the rate of  $H_2$  production is due to the high formation of intermediates at a high concentration of lactic acid [44]. The rate of hydrogen production with the optimized  $Co_4S_3/CdS$  catalyst in the presence of different scavengers was investigated, as displayed in Fig. 6(f). Ethanol (neutral) and triethanolamine (TEA, alkaline) and  $Na_2S/Na_2SO_3$  aqueous solutions were used as the other scavengers in addition to lactic acid (acidic). A high rate of hydrogen production was observed with lactic acid only. The rate of  $H_2$  production was 190, 230, 305 and 12,360  $\mu\text{mol h}^{-1} \text{g}^{-1}$  in the presence of ethanol, triethanolamine,  $Na_2S/Na_2SO_3$  aqueous solutions and lactic acid, respectively.

The photocatalytic activity of optimized  $Co_4S_3/CdS$  (12,360  $\mu\text{mol h}^{-1} \text{g}^{-1}$ ) composite was compared with different photocatalytic materials (Fig. S7).  $H_2$  production rates of  $Co_4S_3$  (188  $\mu\text{mol h}^{-1} \text{g}^{-1}$ ),  $CdS$  (450  $\mu\text{mol h}^{-1} \text{g}^{-1}$ ),  $Co$ -MOF/ $CdS$  (1500  $\mu\text{mol h}^{-1} \text{g}^{-1}$ ),  $Co_3O_4/CdS$  (2000  $\mu\text{mol h}^{-1} \text{g}^{-1}$ ) and mixed  $Co_4S_3 + CdS$  (6075  $\mu\text{mol h}^{-1} \text{g}^{-1}$ ) are lower than optimized  $Co_4S_3/CdS$  composite. We calculated the apparent quantum efficiency (QEs)

for the optimized  $Co_4S_3/CdS$  nanocomposite under visible light irradiation using a 150 W Xe lamp with a 425 nm band pass filter. The quantum yield was estimated to around 1.22%, which is one of the highest QE (%) values than those in earlier reported cobalt sulphide/ $CdS$  nanostructures.

### 3.8. Proposed reaction mechanism

The generation and migration pathways of the charge carrier greatly influence the mechanism of photocatalytic hydrogen production. These charge carrier migration pathways depend on the conduction band potentials of the photocatalytic materials [18]. To determine the exact energy levels for evaluating the conduction band potentials of as-synthesized materials, Mott-Schottky (MS) measurements performed and we determined the feasibility for reduction of  $H^+$  to  $H_2$  (Fig. S4). Based on MS measurements, the conduction band (CB) potentials of  $CdS$  and  $Co_4S_3$  nanocomposites were about  $-1.12$  and  $-0.63$  V vs.  $E_{Ag/AgCl}$ , respectively, at a frequencies of 0.5, 1.0, and 2.0 kHz. Consequently, the CB potential values (vs.  $E_{Ag/AgCl}$ ) were adapted to the normal hydrogen electrode (NHE) scale by  $E_{NHE} = E_{Ag/AgCl} + 0.197$  [44]. We appraised the CB potential values are  $-0.923$  and  $-0.433$  V (vs.  $E_{NHE}$ ) for  $CdS$  (band gap 2.0 eV) and  $Co_4S_3$  (band gap 1.75 eV) respectively. These results clearly specify that the CB potential of  $Co_4S_3$  is very nearer to  $H^+$  reduction potential ( $-0.41$  V vs.  $E_{NHE}$  at pH = 7) [45]. The  $Co_4S_3$  CB potential is very closer to the  $H^+$  reduction potential than that of  $CdS$ , which leads to higher photocatalytic efficiency. A plausible mechanism for the efficient production of  $H_2$  under solar light irradiation with lactic acid as the hole scavenger and  $Co_4S_3/CdS$  as the photocatalyst is depicted in Fig. 7. Excitation of the semiconducting  $CdS$  in  $Co_4S_3/CdS$  by solar light generates electron-hole pairs in the conduction and valence bands, respectively. Then, excited electron is transferred to  $Co_4S_3$  and effectively separates the photogenerated holes, followed by reduction of protons to molecular  $H_2$ . The sacrificial agent (i.e., lactic acid) is oxidized by the photogenerated holes in the valence band of  $CdS$ . However, the  $Co_4S_3/CdS$  composite exhibited superior activity compared to that of the pristine  $CdS$  nanoparticles.  $Co_4S_3$  strongly hinders the recombination of the photogenerated charge carriers and enhances the surface shuttling properties. In addition, the greater number of active edge sites also contributed to the improved adsorption and reduction of protons to produce  $H_2$ .

## 4. Conclusions

Earth-abundant, noble metal-free MOF-derived onion slice-type hollow-structured  $Co_4S_3$  can be used as an efficient co-catalyst with  $CdS$  nanoparticles to achieve extraordinary photocatalytic  $H_2$  production under solar light irradiation. The abundant active sites and the onion slice-type hollow nature is highly beneficial for achieving enhanced energy density due to the higher content of active species. Specifically, zero-dimensional nanoparticles can be readily dispersed in hollow nanostructures and high electrical conductivity of  $Co_4S_3$  leads effective separation of the photogenerated charge carriers and improves the surface shuttling properties. The  $Co_4S_3/CdS$  composites exhibit extremely high photocatalytic activity, showing the highest  $H_2$  production rates ever reported for cobalt sulfide-based composites. Hence, this system provides significant motivation for further research on the conversion of solar energy to chemical fuels.

## Acknowledgments

This work was supported by National Research Foundation of Korea (NRF) grants, funded by the Korean Government (MSIP) (2014R1A4A1001690 and 2016R1E1A1A01941978). This study was also financially supported by the 2017 Post-Doc. Development Program of Pusan National University.

## Appendix A. Supplementary data

Supplementary data associated with this article can be found, in the online version, at <http://dx.doi.org/10.1016/j.apcatb.2017.10.051>.

## References

- [1] A. Paracchino, V. Laporte, K. Sivula, M. Gratzel, E. Thimsen, *Nat. Mater.* 10 (2011) 456–461.
- [2] N.S. Lewis, D.G. Nocera, *Proc. Natl. Acad. Sci. U. S. A.* 103 (2006) 15729–15735.
- [3] D.P. Kumar, M.V. Shankar, M.M. Kumari, G. Sadanandam, B. Srinivas, V. Durgakumari, *Chem. Commun.* 49 (2013) 9443–9445.
- [4] D.P. Kumar, N.L. Reddy, M.M. Kumari, B. Srinivas, V. Durgakumari, B. Sreedhar, V. Roddatis, O. Bondarchuk, M. Karthik, B. Neppolian, M.V. Shankar, *Sol. Energy Mater. Sol. Cells* 136 (2015) 157–166.
- [5] D.P. Kumar, N.L. Reddy, B. Srinivas, V. Durgakumari, V. Roddatis, O. Bondarchuk, M.M. Karthik, Y. Ikuma, M.V. Shankar, *Sol. Energy Mater. Sol. Cells* 146 (2016) 63–71.
- [6] D.P. Kumar, N.L. Reddy, M. Karthik, B. Neppolian, J. Madhavan, M.V. Shankar, *Sol. Energy Mater. Sol. Cells* 154 (2016) 78–87.
- [7] D.P. Kumar, V.D. Kumari, M. Karthik, M. Sathish, M.V. Shankar, *Sol. Energy Mater. Sol. Cells* 163 (2017) 113–119.
- [8] S.G. Babu, R. Vinoth, D.P. Kumar, M.V. Shankar, H.L. Chou, K. Vinodgopal, B. Neppolian, *Nanoscale* 7 (2015) 7849–7857.
- [9] K. Maeda, T. Takata, M. Hara, N. Saito, Y. Inoue, H. Kobayashi, K. Domen, *J. Am. Chem. Soc.* 127 (2005) 8286–8287.
- [10] T. Shimidzu, T. Iyoda, Y. Koide, *J. Am. Chem. Soc.* 107 (1985) 35–41.
- [11] T. Hirai, K. Maeda, M. Yoshida, J. Kubota, S. Ikeda, M. Matsumura, K. Domen, *J. Phys. Chem. C* 111 (2007) 18853–18855.
- [12] L.L. Jensen, J.T. Muckerman, M.D. Newton, *J. Phys. Chem. C* 112 (2008) 3439–3446.
- [13] Q.J. Xiang, J.G. Yu, M. Jaroniec, *Chem. Soc. Rev.* 41 (2012) 782–796.
- [14] Q.J. Xiang, J.G. Yu, *J. Phys. Chem. Lett.* 4 (2013) 753–759.
- [15] J.X. Low, S.W. Cao, J.G. Yu, S. Wageh, *Chem. Commun.* 50 (2014) 10768–10777.
- [16] D.P. Kumar, J. Choi, S. Hong, D.A. Reddy, S. Lee, T.K. Kim, *ACS Sustain. Chem. Eng.* 4 (2016) 7158–7166.
- [17] D.P. Kumar, S. Hong, D.A. Reddy, T.K. Kim, *J. Mater. Chem. A* 4 (2016) 18551–18558.
- [18] D.P. Kumar, S. Hong, D.A. Reddy, T.K. Kim, *Appl. Catal. B* 212 (2017) 7–14.
- [19] D.A. Reddy, H. Park, R. Ma, D.P. Kumar, M. Lim, T.K. Kim, *ChemSusChem* 10 (2017) 1563–1570.
- [20] D.A. Reddy, H.K. Kim, Y. Kim, S. Lee, J. Choi, M.J. Islam, D.P. Kumar, T.K. Kim, *J. Mater. Chem. A* 4 (2016) 13890–13898.
- [21] D.A. Reddy, H. Park, S. Hong, D.P. Kumar, T.K. Kim, *J. Mater. Chem. A* 5 (2017) 6981–6991.
- [22] M. Matsumura, S. Furukawa, Y. Saho, H. Tsubomura, *J. Phys. Chem.* 89 (1985) 1327–1329.
- [23] H.J. Yan, J.H. Yang, G.J. Ma, G.P. Wu, X. Zong, Z.B. Lei, J.Y. Shi, C. Li, *J. Catal.* 266 (2009) 165–168.
- [24] X. Zong, G.P. Wu, H.J. Yan, G.J. Ma, J.Y. Shi, F.Y. Wen, L. Wang, C. Li, *J. Phys. Chem. C* 114 (2010) 1963–1968.
- [25] Y. Yang, H. Yan, X. Wang, F. Wen, Z. Wang, D. Fan, J. Shi, C. Li, *J. Catal.* 290 (2012) 151–157.
- [26] R. Marschall, *Adv. Funct. Mater.* 24 (2014) 2421–2440.
- [27] H. Yan, J. Yang, G. Ma, G. Wu, X. Zong, Z. Lei, J. Shi, C. Li, *J. Catal.* 166 (2009) 165–168.
- [28] J. Yang, D. Wang, H. Han, C. Li, *Acc. Chem. Res.* 46 (2013) 1900–1909.
- [29] C. Han, M.Q. Yang, N. Zhang, Y.J. Xu, *J. Mater. Chem. A* 2 (2014) 19156–19166.
- [30] I.B. Rufus, V. Ramakrishnan, B. Viswanathan, J.C. Kuriacose, *Langmuir* 6 (1990) 565–567.
- [31] M.R. Gao, Y.F. Xu, J. Jiang, S.H. Yu, *Chem. Soc. Rev.* (2013) 2986–3017.
- [32] X.H. Rui, H.T. Tan, Q.Y. Yan, *Nanoscale* 6 (2014) 9889–9924.
- [33] X. Xu, W. Liu, Y. Kim, J. Cho, *Nano Today* 9 (2014) 604–630.
- [34] X. Huang, Z. Zeng, H. Zhang, *Chem. Soc. Rev.* 42 (2013) 1934–1946.
- [35] X.W. Lou, L.A. Archer, Z.C. Yang, *Adv. Mater.* 20 (2008) 3987–4019.
- [36] X. Lai, J.E. Halpert, D. Wang, *Energy Environ. Sci.* 5 (2012) 5604–5618.
- [37] Z. Wang, L. Zhou, X.W. Lou, *Adv. Mater.* 24 (2012) 1903–1911.
- [38] M.H. Oh, T. Yu, S.H. Yu, B. Lim, K.T. Ko, M.G. Willinger, D.H. Seo, B.H. Kim, M.G. Cho, J.H. Park, K. Kang, Y.E. Sung, N. Pinna, T. Hyeon, *Science* 340 (2013) 964–968.
- [39] H. Hu, B.Y. Guan, X.W. Lou, *Chemistry* 1 (2016) 102–113.
- [40] X.Y. Yu, L. Yu, H.B. Wu, X.W. Lou, *Angew. Chem. Int. Ed.* 54 (2015) 5331–5335.
- [41] B.Y. Guan, L. Yu, X. Wang, S.Y. Song, X.W. Lou, *Adv. Mater.* 29 (2017) 1605051.
- [42] D. Lang, F. Cheng, Q. Xiang, *Catal. Sci. Technol.* 6 (2016) 6207–6216.
- [43] W. Zhang, Y. Wang, Z. Wang, Z. Zhong, R. Xu, *Chem. Commun.* 46 (2010) 7631–7633.
- [44] Y. Li, H. Zhang, P. Liu, D. Wang, Y. Li, H. Zhao, *Small* 9 (2013) 3336–3344.
- [45] Q. Xiang, B. Cheng, J. Yu, *Angew. Chem. Int. Ed.* 54 (2015) 11350–11366.
- [46] N. Iqbal, I. Khan, Z.H. Yamani, A. Qurashi, *Sci. Rep.* 6 (2016) 32319.